



Linear vs. nonlinear acceleration in plasma turbulence. II. Hall–finite-Larmor-radius magnetohydrodynamics

Sanjoy Ghosh and Tulasi N. Parashar

Citation: *Physics of Plasmas* **22**, 042303 (2015); doi: 10.1063/1.4916976

View online: <http://dx.doi.org/10.1063/1.4916976>

View Table of Contents: <http://scitation.aip.org/content/aip/journal/pop/22/4?ver=pdfcov>

Published by the AIP Publishing

Articles you may be interested in

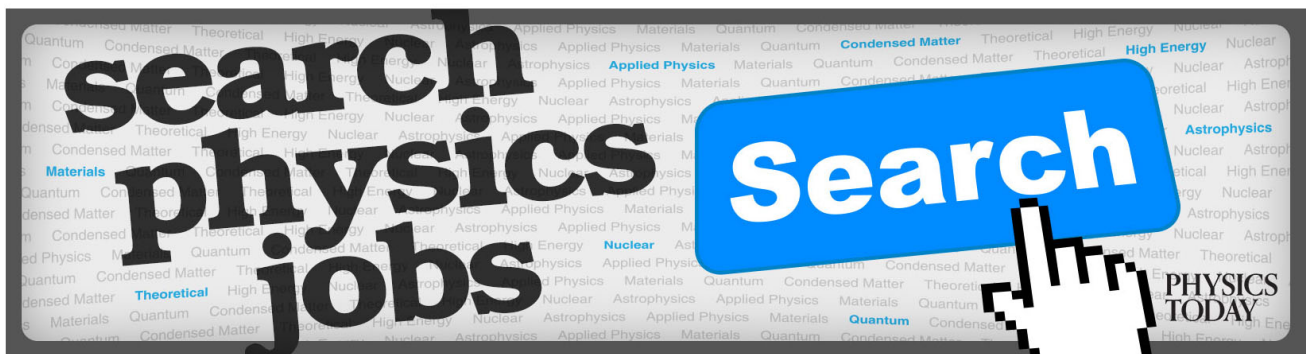
[Linear vs. nonlinear acceleration in plasma turbulence. I. Global versus local measures](#)
Phys. Plasmas **22**, 042302 (2015); 10.1063/1.4916975

[Self-organisation and non-linear dynamics in driven magnetohydrodynamic turbulent flows](#)
Phys. Fluids **27**, 045105 (2015); 10.1063/1.4916971

[Nonlinear finite-Larmor-radius effects in reduced fluid models](#)
Phys. Plasmas **15**, 082302 (2008); 10.1063/1.2965827

[Nonlinear evolution of the \$m = 1\$ internal kink mode in the presence of magnetohydrodynamic turbulence](#)
Phys. Plasmas **13**, 032506 (2006); 10.1063/1.2179772

[Energy fluxes and shell-to-shell transfers in three-dimensional decaying magnetohydrodynamic turbulence](#)
Phys. Plasmas **12**, 042309 (2005); 10.1063/1.1867996



Linear vs. nonlinear acceleration in plasma turbulence. II. Hall–finite-Larmor-radius magnetohydrodynamics

Sanjoy Ghosh¹ and Tulasi N. Parashar²

¹*Johns Hopkins University Applied Physics Laboratory, Laurel, Maryland 20723, USA*

²*University of Delaware, Newark, Delaware 19716, USA*

(Received 10 December 2014; accepted 2 March 2015; published online 9 April 2015)

The local k-space ratio of linear and nonlinear accelerations associated with a variety of initial conditions undergoing steady relaxation is investigated for the Hall–finite-Larmor-radius magnetohydrodynamics (MHD) system in the presence of a mean magnetic field. Building on a related study (Paper I) where it was shown that discrepancies exist between describing the global and local characterizations of the pure MHD system with mean magnetic field, we find regions of the Fourier space that are consistently dominated by linear acceleration and other regions that are consistently dominated by nonlinear acceleration, independent of the overall system's description as linear, weakly nonlinear, or turbulent. In general, dynamics within a certain angular range of the mean magnetic field direction are predominantly linear, while dynamics adjacent the Hall scales along the field-parallel direction and dynamics adjacent the finite Larmor radius scales in the field-perpendicular direction can become strongly nonlinear. The nonlinear influences are particularly significant as the plasma beta increases from unity to higher values. © 2015 AIP Publishing LLC. [<http://dx.doi.org/10.1063/1.4916976>]

I. INTRODUCTION

Solar, astrophysical, and terrestrial plasmas can display linear behavior, fully developed turbulence, or a complicated admixture. As found in any text book, the linear approach under a one-fluid approximation such as magnetohydrodynamics (MHD) can be characterized by small-amplitude expansions around zeroth-order quantities such as the mean density or a mean magnetic field to recover wave-like solutions and dispersion relations between the frequency and wave number of the small-amplitude perturbation. The nonlinear approach typically focuses on three-wave¹ or four-wave² couplings that lead to the development of Kolmogorov-like³ or similar⁴ cascade spectra. The frequency dependence, in the triad/quartic couplings, is neglected on grounds that the time-scale of nonlinear couplings dominates any linear frequency: $\omega_{NL} > \omega_{Lin}$.

In the heliophysics domain, instances where both linear and nonlinear approaches are combined or co-exist are few. Recent examples from the MHD simulations domain include.^{5,6} Critical-balance⁷ can be included from the theoretical side. It has been studied extensively in various simulations models, especially recently in gyrokinetics.⁸ On the other hand and to the best of our knowledge, measurements of the relative strengths of linear and nonlinear influences across the entire Fourier wave vector range from direct numerical simulations have never been investigated. This relatively simple diagnostic is easily obtained from the equations of motion by separating the time-evolution algorithm into their respective linear and nonlinear components. The relative strength of each acceleration term is evaluated across the simulation's entire wave vector space as a function of time.

In Paper I,⁹ we examined the relative strengths of the linear and nonlinear accelerations at each Fourier wave vector as obtained from direct numerical simulations of the pure

MHD system. In this paper, we extend our analysis to the ion-cyclotron scale through inclusion of Hall and Finite-Larmor-Radius (FLR) corrections to the MHD system of equations. Although our focus is heliophysics, and particularly the solar wind, the ideas discussed here are relevant to a broader variety of plasma environments. Our selection of initial states and plasma parameters are consistent with a range of solar wind conditions at 1 AU and the inner heliosphere.

The organization of our paper is as follows. In Sec. II, we present the simulation algorithm, our selection of initial conditions and plasma states, and the representation of the diagnostic terms we use for this study. The simulation results are discussed in Sec. III. A summary and discussion are presented in Sec. IV.

II. SIMULATION DETAILS

A. Equations

Our simulations are based on a standard dimensionless representation of the compressible Hall–FLR MHD system comprising the equations of continuity, momentum, and magnetic induction

$$\frac{\partial}{\partial t} \rho = -\nabla \cdot (\rho \mathbf{u}), \quad (1)$$

$$\begin{aligned} \frac{\partial}{\partial t} \mathbf{u} = & -\mathbf{u} \cdot \nabla \mathbf{u} - \frac{1}{\gamma M_{s0}^2 \rho} \nabla \cdot [\mathbf{P}\mathbf{I} + \epsilon \mathbf{\Pi}] + \frac{\mathbf{J} \times \mathbf{B}}{M_{a0}^2 \rho} \\ & + \frac{1}{\rho} \nu \nabla^2 \mathbf{u} + \frac{1}{\rho} \left(\zeta + \frac{1}{3} \nu \right) \nabla (\nabla \cdot \mathbf{u}), \end{aligned} \quad (2)$$

$$\frac{\partial}{\partial t} \mathbf{B} = \nabla \times \left(\mathbf{u} - \epsilon \frac{\mathbf{J}}{\rho} \right) \times \mathbf{B} - \mu \nabla \times \mathbf{J}. \quad (3)$$

Here, the fluid velocity is \mathbf{u} . The current \mathbf{J} is related to the magnetic field \mathbf{B} and the vector potential \mathbf{A} through $\mathbf{J} = \nabla \times \mathbf{B} = \nabla \times \nabla \times \mathbf{A}$. The magnetic field is composed of a constant plus fluctuations: $\mathbf{B} = \mathbf{B}_0 + \delta\mathbf{B}$, where $\mathbf{B}_0 = B_0 \hat{\mathbf{x}}$. The function F is chosen to preserve the Coulomb gauge condition, $\nabla \cdot \mathbf{A} = 0$ (see, e.g., Ref. 10). The system is closed by using a polytropic relation between pressure and density, $P = \rho^\gamma / (\gamma M_{s0}^2)$, with $\gamma = 5/3$.

The two coefficients M_{s0} and M_{a0} represent a characteristic sonic Mach number and a characteristic Alfvénic Mach number, respectively. The normalization of our Hall–FLR MHD system is formally in eddy turnover units; however, we set $M_{a0} = 1$ to run the simulations in Alfvén speed units. At any time, the average sonic Mach number is $M_s = u_{\text{rms}} / c_{s,\text{rms}} = M_{s0} u_{\text{rms}} / \rho_{\text{rms}}^{(\gamma-1)/2}$, where the rms subscript represents a (spatial) root-mean-square such that $u_{\text{rms}} = [\langle |\mathbf{u}|^2 \rangle_x]^{1/2}$ and $\langle \dots \rangle_x$ denotes a spatial average. The rms sound speed is $c_{s,\text{rms}} = \rho_{\text{rms}}^{(\gamma-1)/2} / M_{s0}$. Since the initial density is unity, $\rho_{\text{rms}}^{(\gamma-1)/2} = 1$ at $T=0$. The average Alfvénic Mach number is $M_a = u_{\text{rms}} / v_{a,\text{rms}} = M_{a0} (\rho_{\text{rms}})^{1/2} u_{\text{rms}} / B_0$, where $v_{a,\text{rms}}$ is the root-mean-square of the (dimensionless) Alfvén speed. Thus, the plasma β , defined as the ratio of squared sound speed to the squared Alfvén speed, becomes $\beta = c_s^2 / v_a^2 = 1 / (M_{s0} B_0)^2$. For the simulations presented in this paper, we choose $M_{s0} = 1/4$. We vary B_0 to sample different plasma β regimes.

The Hall coefficient is $\epsilon \equiv \omega_A / \omega_{ci}$, where $\omega_A = \omega(k_{\min})$ is the (dimensionless) Alfvén frequency of the lowest wave number and ω_{ci} is the ion cyclotron frequency. Hence, the reciprocal of ϵ is the resonant wave number (along \mathbf{B}_0) at which the nondispersive Alfvén frequency resonates with the ion cyclotron frequency.

The FLR pressure tensor (see Ref. 11) is given by the expression, $\epsilon \Pi$, where

$$\begin{aligned}\Pi_{xx} &= 0, \\ \Pi_{yy} &= -\Pi_{zz} = -\frac{P}{2} \left[\frac{\partial u_z}{\partial y} + \frac{\partial u_y}{\partial z} \right], \\ \Pi_{yz} &= \Pi_{zy} = \frac{P}{2} \left[\frac{\partial u_y}{\partial y} - \frac{\partial u_z}{\partial z} \right], \\ \Pi_{zx} &= \Pi_{xz} = P \left[\frac{\partial u_y}{\partial x} + \frac{\partial u_x}{\partial y} \right], \\ \Pi_{xy} &= \Pi_{yx} = -P \left[\frac{\partial u_z}{\partial x} + \frac{\partial u_x}{\partial z} \right],\end{aligned}$$

and Hall term: $\epsilon \mathbf{J}/\rho$. Hence, the Hall term appears purely as a correction to the magnetic induction equation, and the FLR term appears purely as a correction to the momentum equation.

The applicability domain of the pure MHD and Hall–FLR MHD systems is depicted in Figure 1. It shows the k -space ranging from outer scales all the way to sub-electron scales. The largest scales are assumed to be the correlation length, giving us $k_o d_i \sim 10^4$ and $k_o d_e \sim 4.3 \times 10^5$, where d_i (d_e) is the proton (electron) inertial length and k_o is the wavenumber for the outer scale. $k_o d_i = 10^4$ ($\equiv k_o d_e = 1$) relates MHD physics to kinetic physics. Typical systems

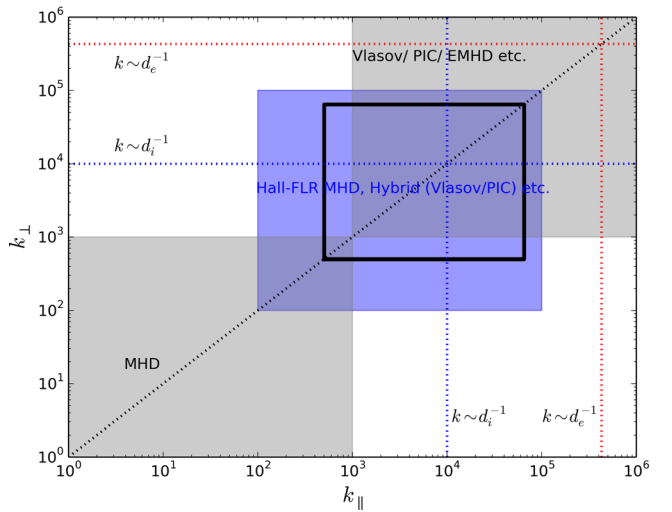


FIG. 1. Range of applicability of different simulation models ranging from pure MHD to electron scale models. The depicted spectral range is typical of the solar wind at 1AU. Different boxes show typical resolvable k modes by most modern simulation models. Proton (d_i) and electron (d_e) inertial lengths are also shown for reference purposes. The simulations discussed in this paper are applicable roughly in the black box shown around $kd_i \sim 1$.

sizes resolvable (in $2\frac{1}{2}$ -D, 3D in rare cases) by most modern simulation models are shown.

The results presented in Paper I apply to the MHD regime. The results of this paper apply to the Hall–FLR (Hybrid Vlasov/Particle-in-Cell) regime shown in blue in Figure 1. The overlap as shown is at the high k values for MHD and the low k values for Hall–FLR MHD.

We implement a pseudospectral algorithm with a predictor-corrector timestepping formalism for our simulations. Details of our approach are available in Refs. 10 and 12. Our primary simulation algorithm is a $2\frac{1}{2}$ -D code run at 256×256 resolution. This permits wave couplings out to the maximum wave number, $|k_{i,\max}| = 128$ for $i = (x, y)$. A typical run time step is $\Delta t = 5 \times 10^{-5}$, hence runs to $T = 8$ entail stepping to $N_{\text{step}} = 1.6 \times 10^5$. The dimensionality $2\frac{1}{2}$ -D signifies vectorial quantities such as \mathbf{u} and \mathbf{A} have all three spatial components, but each component is a function of only two spatial variables, (x, y) . We have run a smaller number of full 3D simulations at 128^3 resolution to confirm the higher resolution, but limit couplings, of the $2\frac{1}{2}$ -D results.

The simulation time T is in units of the characteristic transit time in the simulation box of an Alfvén wave of unit wave number associated with an ambient magnetic field strength of unity. The normalized length of the box is $L_0 = 2\pi$. Hence, the transit time of a characteristic ($k = 1$, $\mathbf{B}_0 = 1$) Alfvén wave across the length of the entire box is $T = L_0 / V_0 = 2\pi$. We can also discuss time intervals in terms of the eddy turnover time unit, $T_E = T / u_{\text{rms}}$. At the start of the simulation, one eddy turnover time unit corresponds to $0.71 T$. This value increases slightly as u_{rms} decreases during the simulation. At the end of a typical run, $T_E \approx 0.9 T$. Prior experience shows that the long-term turbulence properties, such as the development of a stable nonlinear spectrum, are established within a few eddy turnover times. In this paper, we will consider the dynamics in the range $3.5 \leq T_E \leq 5.5$ ($2.5 \leq T \leq 4$).

The last two terms in the momentum equation represent a familiar model of viscous dissipation, involving viscosity coefficients ζ and ν . We set $\zeta=0$ and adopt a simple bi-Laplacian form for the viscosity and the resistivity, which can be expressed in the transform space as

$$\begin{aligned}\nu(k) &= \nu_0[1 + (k/k_{eq})^2], \\ \mu(k) &= \mu_0[1 + (k/k_{eq})^2].\end{aligned}$$

For the cases studied here, we choose $\nu_0 = \mu_0 = 5 \times 10^{-6}$ and $k_{eq} = 1$. This choice keeps the dissipation relatively low over a broad range of the spectrum while maintaining enough damping at the high wave numbers to minimize aliasing errors. The dissipation may be considered purely numerical in the sense that no attempt is made to physically justify its form. Consequently, we focus our attention only on the wave number scales where dissipation is negligible (typically, $|\mathbf{k}| \leq 50$). A broader discussion of the bi-Laplacian dissipation, its impact in terms of modal mechanical and modal magnetic Reynolds numbers, and the selection of the Hall coefficient ϵ can be found in Ref. 12.

B. Initial conditions

Our system, Eqs. (1)–(3), has been extensively tested with a variety of initial conditions and plasma parameters. For Paper I and this paper, we select three initial states. These states are used to initialize either a pure MHD ($\epsilon=0$) or a Hall–FLR MHD ($\epsilon=1/20$) simulation across a range of mean magnetic field strengths that are associated with the plasma β varying from less than unity to greater than unity.

The first initial state is composed of field-aligned velocity shear (VS) structures superposed with field-align Alfvén waves. Here, the velocity shears have their wave vectors parallel to \mathbf{B}_0 , but they spatially vary in the transverse direction so that $\delta\mathbf{u} = \delta\mathbf{u}_{||}(\mathbf{k}_{\perp})$. Field-aligned Alfvén waves are also known as a slab (S) modes in the turbulence community. The resulting two-component model composed of field-aligned velocity shears and slab modes (VS+S) was studied extensively by Ghosh *et al.*¹³ as a candidate initial state of a “wave-like” model of solar wind fluctuations. We select a finite bandwidth for the VS structures and slab modes with range $1 \leq |\mathbf{k}_{\perp}|, |\mathbf{k}_{||}| \leq 5$. The phases are randomly selected at each wave number. The average spatial energy of the VS structures is $\sum_{k_y, k_z} (\delta\mathbf{v} \cdot \delta\mathbf{v})/2 = E_v^{\text{VS}} = 0.5$. The average energy in slab (Alfvénic) fluctuations is $\sum_{k_x} (\delta\mathbf{u} \cdot \delta\mathbf{u} + \delta\mathbf{B} \cdot \delta\mathbf{B})/2 = E_b^{\text{Slab}} + E_v^{\text{Slab}} = E^{\text{Slab}} = 1.0$, where naturally $E_v^{\text{Slab}} = E_b^{\text{Slab}}$ for field-aligned waves. The normalized cross helicity of these modes is $\sigma_{c,k} = 2\mathbf{u}_k \cdot \mathbf{B}_k / (\mathbf{u}_k \cdot \mathbf{u}_k + \mathbf{B}_k \cdot \mathbf{B}_k) = -1.0$, signifying outwardly propagating waves. The amplitudes of both VS and S fluctuations are adjusted so as to impart a k^{-1} initial modal spectral slope. Here and below, we include $\hat{\mathbf{z}}$ and k_z representations with the understanding that such dependencies are present in the full 3D system, but absent in the $2\frac{1}{2}$ -D system.

The second initial state is an isotropic ball of high cross helicity (Hc) fluctuations. These fluctuations are often selected to explore high cross helicity solar wind turbulence. The average spatial energy of the Hc fluctuations is

$\sum_{k_x, k_y, k_z} (\delta\mathbf{v} \cdot \delta\mathbf{v} + \mathbf{B} \cdot \delta\mathbf{B})/2 = E_v^{\text{Hc}} + E_b^{\text{Hc}} = 1.0$. The fluctuations have bandwidth $1 \leq |\mathbf{k}| \leq 4$ and modal spectral slope of k^{-1} . The phases are randomized at each wave number, while keeping the velocity fluctuation aligned with the magnetic fluctuation, so the normalized cross helicity at each wave number is unity: $\sigma_{c,k} = 1.0$. While opposite in sign from the slab waves in the VS+S initial state, the nonlinear evolution of such extremal high cross helicity states are known to be similar.¹⁴

The third (final) initial state we use is an isotropic ball of low cross helicity (Lc) fluctuations. Such fluctuations are often selected to explore low cross helicity solar wind turbulence. The Lc fluctuations are constructed virtually identical to the Hc fluctuations, with the bandwidth, average spatial energy, and spectral slope is identical to the Hc initial state. The normalized cross helicity at each wave vector is adjusted to zero: $\sigma_{c,k} = 0.0$ to enforce low cross helicity at every mode.

The VS+S initial state is composed of explicit well-identified linear waves. Explicit linear waves are less evident in the Hc and Lc initial states, which are typically used for turbulence simulations. The selection choice of these initial states is deliberate: it will be interesting to compare the ratio of nonlinear to linear accelerations from an overtly “wave-like” state such as VS+S against the turbulent states such as Hc and Lc. Moreover, it will be interesting to compare the R_M and R_N ratios between the Hc and Lc runs. The conventional perspective, at least from pure MHD, is that nonlinearities are weaker in high cross helicity states compared to equivalent low cross helicity states.^{14–16}

In all three cases, the initial density is adjusted to eliminate acoustic fluctuations by performing a pseudosound correction to the initial $\rho(k_x, k_y) = 1.0$ density and eliminating all $\nabla \cdot \mathbf{u}$ perturbations at $T=0$ (see Refs. 17 and 18).

We take the above three initial states and run simulations with varying strengths of \mathbf{B}_0 to explore the range $\beta = 1/4$, $\beta = 1$ and $\beta = 4$. Table I summarizes the list of the runs performed for this study.

Broadband turbulence develops from these limited-band initial conditions self-consistently. The dissipation coefficients are set so that dissipation is significant above $|\mathbf{k}| \sim 50$. The Hall scale (ion inertial scale) is $k_e = \omega_{ci}/V_A = 20$. The FLR scale varied from simulation to simulation as $k_L = \omega_{ci}/V_{th} = k_e/\beta^{1/2}$.

TABLE I. Table showing the details of different runs.

Run	β	Initial condition
1a	0.25	Alfven waves + VS+S
1b	0.25	Hc helicity noise
1c	0.25	Lc helicity noise
2a	1	Alfven waves + VS+S
2b	1	Hc helicity noise
2c	1	Lc helicity noise
3a	4	Alfven waves + VS+S
3b	4	Hc helicity noise
3c	4	Lc helicity noise

Each run listed in Table I is representative of a larger family of simulations we performed, but do not present. For the VS+S initial state, we ran cases with different selections of VS structures bandwidth and S (Slab) fluctuation wave numbers. For the Lc and Hc initial states, we changed the range of initial bandwidth and as well as different selections of random phases. Our results did not change significantly with these alternate selections.

C. Diagnostics

As in Paper I, we compute the relative strength of linear to nonlinear accelerations at each Fourier wave vector. Here, we repeat the details for the sake of completeness. The right hand sides of the momentum equation and the induction equation are separated into linear, nonlinear, and dissipative acceleration terms

$$\begin{aligned}\frac{\partial \mathbf{u}}{\partial t} &= \mathbf{N} = \mathbf{N}_{Lin} + \mathbf{N}_{NL} + \mathbf{N}_{diss}, \\ \frac{\partial \mathbf{B}}{\partial t} &= \mathbf{M} = \mathbf{M}_{Lin} + \mathbf{M}_{NL} + \mathbf{M}_{diss}.\end{aligned}$$

Our choice of the **N** and **M** lettering is motivated by **N** representing the Navier-Stokes acceleration component and **M** representing the magnetic [field] acceleration component. The exact representations of the linear accelerations at each time step, \mathbf{N}_{Lin} and \mathbf{M}_{Lin} , are easily extracted from the general predictor-corrector time-stepping scheme of our simulation algorithms by retaining only the zero-th and first order terms of **N** and **M** while setting the dissipation terms to zero. The nonlinear accelerations are recovered by computing $\mathbf{N}_{NL} = \mathbf{N} - \mathbf{N}_{Lin}$ and $\mathbf{M}_{NL} = \mathbf{M} - \mathbf{M}_{Lin}$, with, again, the dissipation terms set to zero. Please refer to Paper I for more details of how these quantities are computed.

We then compute the ratio of linear and nonlinear accelerations

$$\begin{aligned}R_N(k_x, k_y) &= \frac{\langle N_{NL}(k_x, k_y, t) \rangle_{\Delta T}}{\langle N_{Lin}(k_x, k_y, t) \rangle_{\Delta T}}, \\ R_M(k_x, k_y) &= \frac{\langle M_{NL}(k_x, k_y, t) \rangle_{\Delta T}}{\langle M_{Lin}(k_x, k_y, t) \rangle_{\Delta T}},\end{aligned}\quad (4)$$

where N_{NL} and N_{Lin} are the magnitudes of the vectors \mathbf{N}_{NL} and \mathbf{N}_{Lin} , respectively, and the same applies for the quantities R_M , M_{NL} , and M_{Lin} . The angled brackets $\langle \dots \rangle_{\Delta T}$ represent a time-averaging over some specified time interval sampled at some specified cadence.

We have investigated R_N and R_M at a variety of time resolutions ranging from the simulation time step, $\Delta t = 5 \times 10^{-5}$, to fast magnetosonic (ms) time scales, which in units of our Alfvén speed normalization, is $\omega_{ms} = B_0 k_{\parallel} [1 + \beta]^{1/2}$, to nonlinear time scales, T_E . After the first few nonlinear times, the power spectrum settles to a state of steady relaxation and the R_N and R_M values settle consistently to a range of values inside of well-defined regimes. Aside from brief random transients where a small cluster of Fourier mode may register R_N or R_M values either less than or greater than unity while the broader region remains concentrated to a more limited range, there are no substantial differences

between the time-instantaneous (R_N , R_M) ratios and the time-averaged ratios. While a complete time-series analysis requires frequency spectra at each \mathbf{k} -mode, we have found little difference between time-averaging the acceleration ratios across magnetosonic, Alfvénic, or nonlinear time scales. Consequently, we present the long-term values R_N and R_M in the discussion below using the same cadence and time-averaging interval as in Paper I: $2.5 \leq T \leq 4$ sampled at every quarter simulation time $\Delta T = 0.25$. In nonlinear time units T_E , this is equivalent to averaging across roughly two eddy turnover time intervals $3.5 \leq T_E \leq 5.5$ at a cadence of $\Delta T_E \sim 0.3$.

While the quantities R_N and R_M measure the magnitude ratios of the nonlinear and linear accelerations, it is important to also check the relative alignments of the acceleration vectors. For this, we define alignment angles θ_{LN}^N and θ_{LN}^M defined as

$$\begin{aligned}\cos(\theta_{LN}^N) &= \left\langle \frac{\mathbf{N}_{Lin} \cdot \mathbf{N}_{NL}}{[N_{Lin}^2 + N_{NL}^2]^{1/2}} \right\rangle_{\Delta T}, \\ \cos(\theta_{LN}^M) &= \left\langle \frac{\mathbf{M}_{Lin} \cdot \mathbf{M}_{NL}}{[M_{Lin}^2 + M_{NL}^2]^{1/2}} \right\rangle_{\Delta T}.\end{aligned}\quad (5)$$

Here, the θ subscript *LN* refers to the linear (*L*) and nonlinear (*N*) accelerations, and the superscripts *N* and *M* refer to the accelerations: Navier-Stokes (*N*) or magnetic field (*M*). These alignment angles are reminiscent of the θ_{uB} alignment angle between the velocity **u** and the magnetic field **B** that is used to investigate cross helicity alignments. The angled brackets $\langle \dots \rangle_{\Delta T}$ again denote a time-averaging. We note that the meaning of a time-averaged alignment angle is somewhat unclear depending on the time interval and cadence with which the averaging is performed. Regardless, if a strong alignment or anti-alignment (e.g., $\cos(\theta_{LN}^N) \sim +1$ or $\cos(\theta_{LN}^N) \sim -1$) appears in the time-averaged quantity for a variety of averaging intervals and cadences, it is reasonable to assume that the two vectors are correlated at all times.

Spectral anisotropies are quantifiably described using an anisotropy angle. The anisotropy angle is defined as $\Theta_Q \equiv \tan^{-1} \{ (\sum_k k_{\perp}^2 |Q(\mathbf{k}, t)|^2 / \sum_k k_{\parallel}^2 |Q(\mathbf{k}, t)|^2)^{1/2} \}$, where Q is any physical quantity of interest ranging from a scalar such as density ρ to a vector such as velocity **u** or magnetic field **B** (Ref. 1). Θ_Q gives an estimate of how the energy is distributed in k_{\perp} and k_{\parallel} . Here, the summations extend over all values of \mathbf{k} . Hence, while Θ_Q provides information on the overall anisotropy measure of a turbulent system, it does not distinguish between changes in relative anisotropy across large and small scales. We find it convenient to define the relative anisotropy of various quantities in terms of a spectral anisotropy angle $\theta(k)$ defined as

$$\tan^2 \theta_Q(k) = \frac{\sum_{\Delta k} k_{\perp}^2 \langle |Q(\mathbf{k}, t)|^2 \rangle_{\Delta T}}{\sum_{\Delta k} k_{\parallel}^2 \langle |Q(\mathbf{k}, t)|^2 \rangle_{\Delta T}},\quad (6)$$

where the summations are over annulae $|\mathbf{k}| - \frac{1}{2} \leq \Delta k < |\mathbf{k}| + \frac{1}{2}$ for $|\mathbf{k}| = 1, 2, 3, \dots, 128$, \mathbf{k} is restricted to the first quadrant of Fourier space, and the angled brackets denote a time average.

III. RESULTS

We now present the results of simulating the initial conditions and plasma states listed in Table I through the Hall–FLR MHD ($\epsilon = 1/20$) simulations. Before exploring the complete study parameter range, we consider the power spectra and spectral anisotropies from these simulations to confirm they are similar to previous work.

Figure 2 shows the time-averaged modal omnidirectional magnetic power spectrum $E_B(k)$ and spectral anisotropy angle $\theta_B(k)$ for three Hall–FLR MHD simulations run at $\beta=1$ (Runs (2a)–(2c)). The three different curves represent the three initial conditions: VS+S, Hc helicity, and Lc helicity. We plot a reference $k^{-8/3}$ line that is representative of a Kolmogorov-like $k^{-5/3}$ spectrum scaled to modal power. The time-averaging is performed using seven snapshots during $2.5 \leq T \leq 4$ simulation times at a cadence of $\Delta T = 0.25$. Choosing this time interval avoids any spectral transients that may occur as the turbulence cascade establishes itself during early nonlinear times, $T_E \lesssim 2$. The vertical black line represents the Hall scale ($k_\epsilon = 20$). The spectral anisotropy angle of the magnetic fluctuations $\theta_B(k)$ shows increased anisotropy at high k for all three initial states leading up to k_ϵ . Plots of $\theta_B(k)$ for $\beta = 1/4$ (not shown) also show enhanced anisotropies leading up to the Hall–FLR scales. While the energy cascade implications for the full Hall–FLR system is reserved for a future paper, we note that these results are

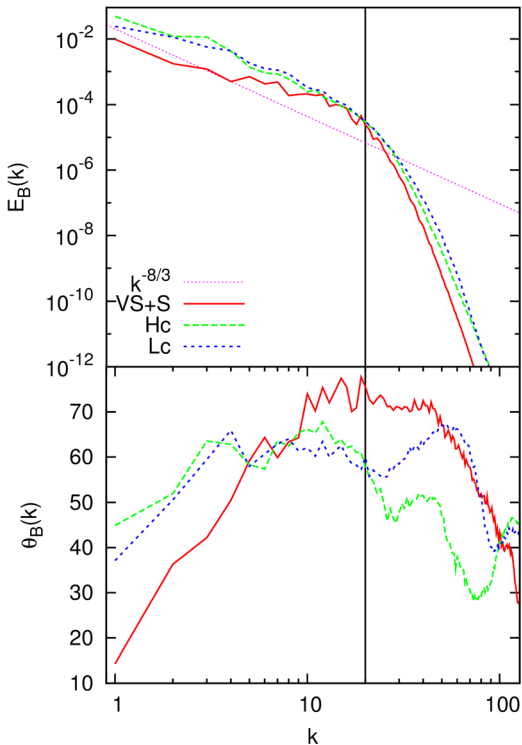


FIG. 2. Modal magnetic spectra and magnetic anisotropy angles for the VS+S (solid red line), Hc (long-dashed green line), and Lc (short-dashed blue line) initial states run using the Hall–FLR ($\epsilon = 1/20$) MHD system with plasma $\beta = 1$. A reference $k^{-8/3}$ (dotted pink) line represents the Kolmogorov prediction. The modal magnetic power steepens at the ion inertial scale $k_\epsilon = 20$, and enhanced anisotropy angles appear with increasing k for the VS+S and Lc cases.

consistent with the anisotropies reported for pure MHD with VS+S initial conditions^{13,19} and for Hall MHD (FLR contribution neglected) by Ghosh and Goldstein.²⁰ Note, the break at the Hall scale is not due to dissipation, but rather the presence of the Hall term. In short, the long-term evolution of all our simulations gives rise to turbulent cascade spectra with, generally speaking, enhanced spectral power in directions perpendicular to the mean magnetic field.

In the discussion that follows, we focus on time-averaged plots of R_N and R_M in the first quadrant of the Fourier space. As with the pure MHD system of Paper I, our initial conditions are symmetric across the $k_y = 0$ axis, and we have not found any substantial morphological difference between the first Fourier space quadrant ($(k_x, k_y) > 0$) and the fourth Fourier space quadrant ($k_x > 0, k_y < 0$), during turbulent relaxation of our Hall–FLR MHD system. To maintain consistency of color scale across all our figures, we clip the color range of R_N and R_M to $0 \leq (R_N, R_M) \leq 2$. That is, values of $(R_M, R_N) \geq 2$ are colored the same as $(R_M, R_N) = 2$. As many as 5% of the red points represent $(R_M, R_N) \geq 2$.

In Paper I, we discussed how \mathbf{k} -space regions of high R_N and R_M are not necessarily regions where spectral energies are large. We went on to show R_M and R_N and the corresponding E_v and E_b energy spectra from a pure MHD case (VS+S $\beta = 1$) case. This figure, Figure 3 of Paper I, is representative of all the pure MHD and Hall–FLR MHD runs we have performed. Consequently, we do not present the equivalent Hall–FLR MHD figure in this paper.

We now present the results of taking the initial conditions and plasma states listed in Table I, running $2\frac{1}{2}$ -D Hall–FLR MHD simulations, and evaluating R_N and R_M in the first Fourier space quadrant after the development of a steady state nonlinear cascade spectrum. This is shown in Figure 3. The equivalent figure for the pure MHD cases appears as Figure 4 of Paper I. The time-averaging and other analysis parameters are identical to those in Paper I. We have inserted a vertical line to identify the Hall (ion inertial) scale at $k_\parallel = k_\epsilon = 20$ and a horizontal line to identify the FLR scale $k_L = \omega_{ci}/V_{th} = k_\epsilon/\beta^{1/2} = 20/\beta^{1/2}$. Similar to Paper I, we insert two reference lines based on predictions on how strong and weak turbulence is ordered across \mathbf{k} -space. The $k_\perp \propto k_\parallel^{3/2}$ relation is predicted by Higdon,²¹ and $k_\perp \propto k_\parallel^2$ relation is predicted by Boldyrev and collaborators.^{22,23}

Surveying across plasma β , Figure 3 shows the strongest ratios of nonlinear-to-linear accelerations occur in R_M adjacent the $k_\perp \gtrsim k_L$ scales for $\beta = 1$ and $\beta = 4$. Here, $R_M \sim 2$.

Strong values of R_M also appear adjacent the Hall resonance at $k_\parallel = k_\epsilon$ and a wide range of k_\perp for VS+S and Hc at $\beta = 4$. Weaker, but still discernable, values ($R_M \sim 1$) appear at $\beta = 1$ and $\beta = 1/4$ for these cases. On the other hand, Lc shows $R_M \sim 1$ in this regime only for $\beta = 4$. These results are consistent with previous work on Hall MHD (FLR contribution absent),^{12,20} where the presence of the Hall term suppressed energy cascades for k_\parallel greater than the Hall resonance at k_ϵ for high cross-helicity states, but not for low cross-helicity states.

The next noticeably strongest values appear as $R_N \sim 1$ and $R_M \sim 1$ that run parallel the k_L and k_ϵ resonance lines. Representative examples include R_N for Lc $\beta = 4$ and R_M for

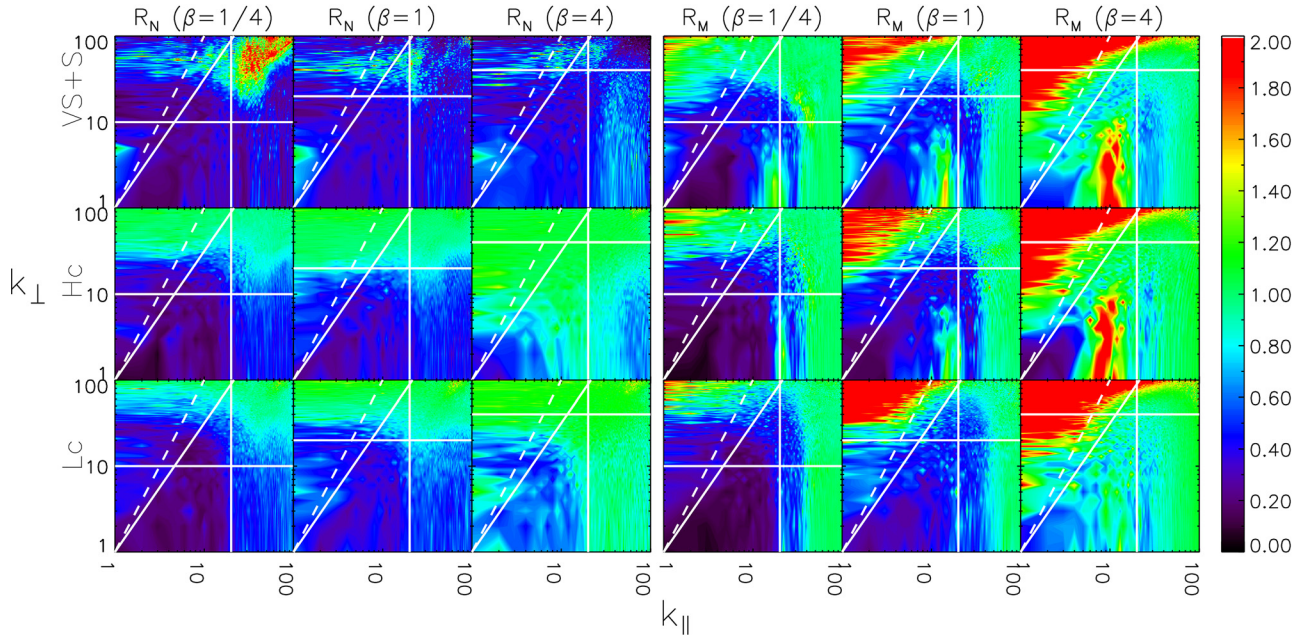


FIG. 3. Time-averaged nonlinear-to-linear acceleration ratios R_N and R_M from the set of Hall–FLR MHD simulations in Table I. Only the first quadrant in Fourier space is shown. The $(k_{\parallel}, k_{\perp})$ axes are logarithmic. The time-averaged R_N from the VS+S, Hc, and Lc initial conditions for $\beta = \frac{1}{4}, 1, 4$ are assembled into a 3×3 set. The time-averaged R_M are arranged similarly. The acceleration ratios are time-averaged using seven time snapshots during $2.5 \leq T \leq 4$. The solid white line identifies $k_{\perp} \sim k_{\parallel}^{3/2}$, the Higdon prediction. The dashed white line identifies $k_{\perp} \sim k_{\parallel}^2$, the Boldyrev prediction. The vertical white line identifies the Hall scale at $k_{\parallel} = k_{\perp} = 20$. The horizontal white line identifies the FLR scale $k_L = \omega_{ci}/V_{th} = k_{\parallel}\beta^{1/2} = 20/\beta^{1/2}$. The R_M ratio shows enhancements adjacent the Hall resonance especially for the VS+S and Hc cases. Both R_N and R_M ratios show enhancements adjacent the FLR resonance.

Hc at $\beta = 1/4$. Here, the boundaries of strong R_N and R_M do not follow the Higdon prediction. This is perhaps understandable since the Higdon formulation is for pure MHD and the region of applicability of the Hall–FLR model is in a different regime of the Fourier space (recall Figure 1).

As with pure MHD case in Paper I, there are aspects of Hall–FLR as depicted in Figure 3 that are interesting:

- (1) R_M is consistently greater than R_N for $\beta = 1$ and $\beta = 4$, regardless of initial state. Similar to Paper I, despite the ratio being larger, the Navier–Stokes dynamics still dominate among the energy-containing modes.
- (2) Although the FLR term is in the momentum equation, it appears to enhance nonlinear accelerations over linear accelerations in R_M adjacent the k_L line. This is confirmed

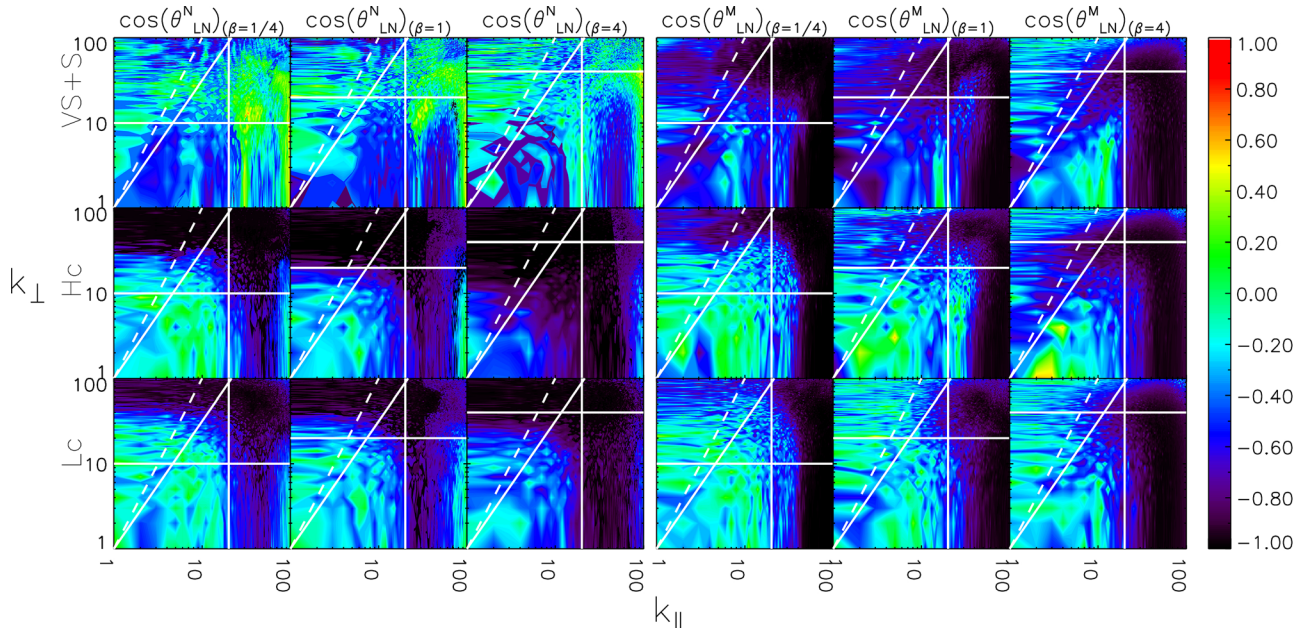


FIG. 4. Time-averaged alignment angles, $\cos(\theta_{LN}^N)$ and $\cos(\theta_{LN}^M)$, associated with Figure 3. Strong anti-alignments, $\cos(\theta_{LN}^N) \sim -1$ or $\cos(\theta_{LN}^M) \sim -1$, often appear where R_N or R_M are of order unity in Figure 3.

by intercomparing the relevant panels between Figure 4 from Paper I and Figure 3 from this paper. Similarly, although not as strong, the Hall term in the magnetic induction equation appears to enhance R_N adjacent the k_e line.

- (3) Comparing the linear-wave dominated VS+S case against the Hc and Lc cases, we notice that the FLR contribution does not lead to significant enhancements in R_N for VS+S as compared to Hc and Lc for all plasma β . Most of the nonlinear enhancements appear through R_M across both k_e and k_L scales for VS+S. This contrasts with the pure MHD model (Paper I), where enhanced R_N appears above the Higdon prediction for VS+S. On the other hand, keeping in mind the relative placements of the pure MHD and the Hall–FLR models in k -space (Figure 1), we do see traces of inertial-range R_N enhancements adjacent $5 \leq k_\perp < 10$ for VS+S in Figure 3.

We next present the cosine of the alignment angles, $\cos(\theta_{LN}^N)$ and $\cos(\theta_{LN}^M)$, associated with Figure 3. This is shown in Figure 4. As discussed, these are time-averaged quantities, and care is needed for their interpretation. Nevertheless, we find a remarkable correlation: Regions where R_N or R_M are of order unity in Figure 3 exhibit strong anti-correlation in their associated value of $\cos(\theta_{LN}^N)$ or $\cos(\theta_{LN}^M)$. Oddly, this correlation does not extend to the strongest R_M values: the regions where $R_M \sim 2$ in Figure 3 ($\beta = 1$ and $\beta = 4$) show no significant anti-correlation in $\cos(\theta_{LN}^M)$.

Alignment angles were also discussed in Paper I. Significant anti-correlations appear in $\cos(\theta_{LN}^N)$ wherever $R_N \sim 1$ in Paper I. This is especially true for the VS+S case across the entire range of plasma β , and to a lesser degree for Hc and Lc at $\beta = 4$.

A common concern with $2\frac{1}{2}$ -D simulations of turbulence is the absence of out of plane couplings. Due to computational and time limitations, we have focused on the $2\frac{1}{2}$ -D model; however, we conducted a few fully 3D simulations. Figure 5 shows R_N and R_M from a pure 3D MHD

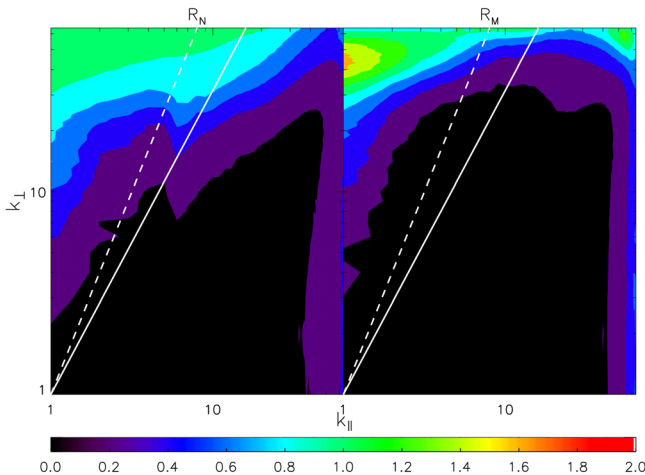


FIG. 5. R_M , R_N for a pure 3D MHD simulation run at 128^3 resolution with VS+S as initial condition, $\beta = 1/4$. The values of R_M and R_N have been averaged in the k_\perp direction in this case to facilitate a qualitative comparison with the $2\frac{1}{2}$ -D case. The solid white line identifies $k_\perp \sim k_\parallel^{3/2}$, the Higdon prediction. The dashed white line identifies $k_\perp \sim k_\parallel^2$, the Boldyrev prediction.

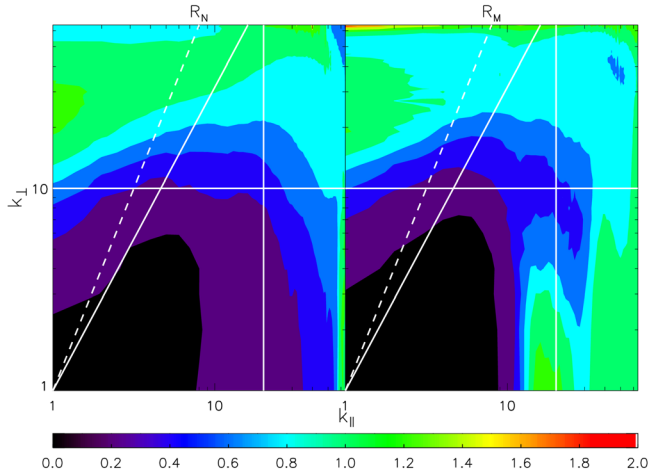


FIG. 6. R_M , R_N for a 3D Hall–FLR MHD simulation run at 128^3 resolution with VS+S as initial condition, $\beta = 1/4$ and $\epsilon = 1/20$. The values of R_M and R_N have been averaged in the k_\perp direction in this case to facilitate a qualitative comparison with the $2\frac{1}{2}$ -D case. The solid white line identifies $k_\perp \sim k_\parallel^{3/2}$, the Higdon prediction. The dashed white line identifies $k_\perp \sim k_\parallel^2$, the Boldyrev prediction.

simulation run at 128^3 resolution. The time-averaged interval and other parameters are the same as in the $2\frac{1}{2}$ -D model. The system is initialized with VS+S initial conditions with phases randomly selected at each wave number. Similar to the $2\frac{1}{2}$ -D, the energy in VS structures, now distributed across the $k_y - k_z$ plane, is $E_v^{\text{VS}} = 0.5$ and $E^{\text{Slab}} = 1.0$. The coefficients for the bi-Laplacian viscosity and resistivity are increased to $\nu_0 = \mu_0 = 5 \times 10^{-5}$ to preserve numerical stability. Beyond this adjustment, the 3-D code is run virtually the same as the $2\frac{1}{2}$ -D code. The extension to 3D Hall–FLR is shown in Figure 6. Here, as before, $\epsilon = 1/20$.

Results from the 3D runs are qualitatively similar to the $2\frac{1}{2}$ -D results. Both R_N and R_M display enhanced nonlinear accelerations above the Higdon prediction in the pure MHD case. Enhancements of R_N and R_M do not follow the Higdon prediction in the Hall–FLR case. There are R_M enhancements adjacent the Hall resonance at $k_\parallel = 20$.

IV. CONCLUSIONS

Magnetofluid turbulence is an important part of plasma dynamics in solar, terrestrial, as well as astrophysical plasmas. In the presence of a large scale magnetic field, plasma turbulence exhibits anisotropy in \mathbf{k} space. This anisotropy is traditionally quantified by the Shebalin anisotropy angle θ_{KB} and the Higdon–Boldyrev predictions.

In a set of papers, Paper I and the present, we have developed and presented a new measure of the plasma turbulence anisotropy. The ratio of nonlinear acceleration to the linear acceleration in the momentum (R_N) as well as induction (R_M) equations was investigated throughout \mathbf{k} space. Nonlinearities dominate in the high k_\perp region of the \mathbf{k} space. In the inertial range (pure MHD, Paper I), the Higdon–Boldyrev predictions delineate the nonlinear regions, but at kinetic scales (Hall–FLR, this paper), we see departures from these predictions as the nonlinearities leak out of this region and become correlated with the Hall (k_e) and FLR (k_L) resonances.

The large values of R_M at the Hall scale imply that the magnetic acceleration is primarily nonlinear adjacent to the dissipation scales. This has important implications for collisionless plasmas such as the solar wind because the dissipation processes must involve interactions between particles and electromagnetic fields.

The presence of enhanced nonlinearities inconsistent with the Higdon–Boldyrev predictions through the inclusion of higher order effects suggests that the traditional theories of turbulence cannot be trivially extended to kinetic scales. Self-consistent theories of turbulence in the kinetic regimes are required.

The nature of these results does not change qualitatively in 3D. However, there may be quantitative differences that will require a systematic study with higher resolution 3-D simulations.

An unexpected result from the Hall–FLR model is that angles between the linear accelerations, \mathbf{N}_{Lin} and \mathbf{M}_{Lin} , and the respective nonlinear accelerations, \mathbf{N}_{NL} and \mathbf{M}_{NL} , are often strongly anti-aligned at the kinetic scales. It is not clear whether this is a spurious result, given the k -space proximity of the dissipation scales in our simulations and the applicability of the Hall–FLR model at these scales. This will need to be further investigated with models more suitable for these scales.

A self consistent kinetic treatment of the problem is required in order to confirm some of the above conclusions. That is the subject of a follow-up paper that will discuss these results using hybrid particle in cell simulations that treat protons as particles and electrons as a neutralizing fluid.

ACKNOWLEDGMENTS

S.G. was supported in part by a Stuart S. Janney Fellowship at JHU APL for this work. T.N.P. was supported

by the NSF Solar Terrestrial Program Grant No. AGS-1063439 and SwRI Subcontract No. D99031L to University of Delaware. Both would like to thank W. H. Matthaeus for useful discussions.

- ¹J. Shebalin, W. Matthaeus, and D. Montgomery, *J. Plasma Phys.* **29**, 525 (1983).
- ²S. Sridhar, *Pramana* **77**, 185 (2011).
- ³A. N. Kolmogorov, Dokl. Akad. Nauk SSSR **30**(4), 299 (1941).
- ⁴R. H. Kraichnan, *Phys. Fluids* **8**, 1385 (1965).
- ⁵P. Dmitruk, W. H. Matthaeus, and L. J. Lanzerotti, *Geophys. Res. Lett.* **31**, L21805, doi:10.1029/2004GL021119 (2004).
- ⁶S. Ghosh, D. Thomson, W. Matthaeus, and L. Lanzerotti, *J. Geophys. Res.* **114**, A08106, doi:10.1029/2009JA014092 (2009).
- ⁷P. Goldreich and S. Sridhar, *Astrophys. J.* **438**, 763 (1995).
- ⁸G. G. Howes, S. C. Cowley, W. Dorland, G. W. Hammett, E. Quataert, and A. A. Schekochihin, *Astrophys. J.* **651**, 590 (2006).
- ⁹S. Ghosh and T. N. Parashar, *Phys. Plasmas* **22**, 042302 (2015).
- ¹⁰S. Ghosh, M. Hossain, and W. H. Matthaeus, *Comput. Phys. Commun.* **74**, 18 (1993).
- ¹¹N. Yajima, *Prog. Theor. Phys.* **36**, 1 (1966).
- ¹²S. Ghosh, E. Siregar, D. A. Roberts, and M. L. Goldstein, *J. Geophys. Res.* **101**, 2493, doi:10.1029/95JA03201 (1996).
- ¹³S. Ghosh, W. Matthaeus, D. Roberts, and M. Goldstein, *J. Geophys. Res.* **103**, 23691, doi:10.1029/98JA02195 (1998).
- ¹⁴A. C. Ting, D. Montgomery, and W. H. Matthaeus, *Phys. Fluids* **29**, 3261 (1986).
- ¹⁵R. Grappin, U. Frisch, A. Pouquet, and J. Leorat, *Astron. Astrophys.* **105**, 6 (1982).
- ¹⁶S. Ghosh, W. Matthaeus, and D. Montgomery, *Phys. Fluids* **31**, 2171 (1988).
- ¹⁷S. Ghosh and W. Matthaeus, *Phys. Fluids A* **4**, 148 (1992).
- ¹⁸W. Matthaeus, S. Ghosh, S. Oughton, and D. Roberts, *J. Geophys. Res.* **101**, 7619, doi:10.1029/95JA03830 (1996).
- ¹⁹S. Ghosh, W. Matthaeus, D. Roberts, and M. Goldstein, *J. Geophys. Res.* **103**, 23705, doi:10.1029/98JA02194 (1998).
- ²⁰S. Ghosh and M. Goldstein, *J. Plasma Phys.* **57**, 129 (1997).
- ²¹J. Higdon, *Astrophys. J.* **285**, 109 (1984).
- ²²S. Boldyrev, *Astrophys. J. Lett.* **626**, L37 (2005).
- ²³S. Boldyrev, *Phys. Rev. Lett.* **96**, 115002 (2006).